Polarization-Driven Topological-Insulator Transition for Piezotronic Field-Effect Transistors with Subthreshold Swing of 5 mV/decade

Chenhao Liang,[1,†] Ruhao Liu,[1,†] Minjiang Dan,[1] Nian Liu,[1] and Yan Zhang [1,2,3,*]

[1] *School of Physics, University of Electronic Science and Technology of China, Chengdu 610054, China*

[2] *Beijing Institute of Nanoenergy and Nanosystems, Chinese Academy of Sciences, Beijing 100083, China*

[3] *College of Nanoscience and Technology, University of Chinese Academy of Sciences, Beijing 100049, China*

A piezotronic field-effect transistor device based on a topological insulator (TI) is proposed based on wurtzite/zincblende InAs quantum wells (QWs). The subthreshold swing can reach 5 mV/decade. The subthreshold swing of FETs requires at least a 60 mV gate voltage due to the thermal voltage. Polarization in these QWs can drive a large-gap TI with a bulk band gap of approximately 50 meV. The TI maintains a large band gap characteristic under a compressive stress of 7 GPa.

I. INTRODUCTION

Piezotronic transistors based on third-generation semiconductor materials, such as ZnO, GaN, and CdS, have advanced applications in multifunctional sensing systems, self-powered electronics, and energy harvesting [1–3]. By coupling piezoelectric, semiconductor, and photon excitations, strain-induced piezoelectric charges can effectively control the properties of carrier generation, recombination, and transport [4–6]. High-performance piezotronic devices have been developed, including nanogenerators [7], strain sensors [8], strain-gated field-effect transistors (FETs) [9], and LEDs [10]. A tactile imaging matrix was achieved based on a taxel-addressable integrated ZnO nanowire array [11]. An atomically thin ZnO piezophototronic device achieved a high photoresponsivity of 300 AW^{-1}, which gained an enhancement of 230% [12]. Topological insulators (TIs) have low-power topological surface states and ultrahigh on:off ratios of up to 10^{10} [13]. The polarization can not only trigger topological phase transition [14], but also induce large spin-orbit coupling over 83 meV/nm^{-1} for potential application of spin qubits [15].

Subthreshold swing is a key parameter of FETs [16]. In conventional FETs based on metal-oxide semiconductor contacts, the Boltzmann tyranny limits the subthreshold swing, which cannot be lower than 60 mV/decade. Negative capacitance and tunneling effects can be used to overcome the subthreshold swing limitation [17]. The approaches to obtain subthreshold swing lower than 60 mV/decade, such as the negative capacitance of ferroelectric insulators [18] and tunneling FETs [17,19], face great challenges in fabrication and performance. Recently, theoretical studies have proposed that the topological quantum field effect may overcome this limitation in two-dimensional (2D) TIs based on Xene materials [20]. However, experimentally grown high-quality Xene still has challenges [21,22].

The III-V compound quantum wells (QWs) beyond the one-dimensional nanowire geometry extend the spatial dimension of high-performance FETs and are desired [23]. Recently, wurtzite/zincblende (WZ/ZB) InAs QWs, with around 150-nm width and 1-μm length, were grown by metalorganic vapor phase epitaxy [24]. Moreover, a WZ III-V film, with arbitrary dimensions, can be grown on the ZB substrate. A WZ [0001] film with a diameter of more than 10 μm was grown on a ZB [111] substrate [25]. In WZ/ZB InAs quantum wells, the basic polytype structure was WZ in the [0001] direction and ZB in the [111] direction [26–28]. Moreover, high-quality WZ/ZB InAs quantum wells were achieved with misplaced bilayers accounting for only 2% of 60 periods of alternating WZ and ZB. The thickness of each layer was 2 nm (equal to eight bilayers of In and As) [29].

In this paper, we propose a way to design a high-performance quantum piezotronic device based on a wurtzite/zincblende InAs quantum well topological insulator. The subthreshold swing for this device can be reduced to 5 mV/decade under a 7-GPa stress. Polarization in WZ/ZB InAs QWs can drive a topological phase transition. The TI has a band gap of over 50 meV, which is wide enough for room-temperature applications. Moreover, FET devices based on this TI system are robust to magnetic perturbation.

*zhangyan@uestc.edu.cn

†These authors contributed equally to this work.

II. THEORY AND METHODS

In Fig. 1(a), we design a split gate structure on the WZ/ZB InAs QWs. The split gates act as a constriction and form a quantum point contact (QPC) [30]. In WZ/ZB InAs QWs, InAs is grown along the [0001] orientation for the WZ phase and along the [111] orientation for the ZB phase [26,31], as shown in Fig. 1(b). A strong polarization P_0 (experimental value 0.002–0.080 C/m^2 [28]) drives band inversion in the QWs and triggers a topological insulator [32]. The width of the QPC W_{QPC} can be controlled by the gate potential on the split gates; therefore, the *on* and *off* of the edge current channels can be manipulated by the gate potential.

According to Refs. [4,33,34], piezoelectric polarization in the QW can be obtained from $P_i = e_{ijk} \cdot S_{jk}$ and the constituting equations as follows:

$$\begin{aligned} \sigma &= C_E S - e_E^T E, \\ D &= e_E S + \kappa E, \end{aligned} \quad (1)$$

where P and S are the polarization vector and strain vector, respectively; e_{ijk} is the piezoelectric tensor; e_E^T is the transposed matrix of e_E. σ and C_E represent the stress and elasticity tensors, respectively; D and E are the electric field and displacement, respectively; and κ is the dielectric tensor. The total polarization ($P = P_{piezo} + P_0$) is the sum of the piezoelectric polarization P_{piezo} induced by external stress and P_0 induced by mismatch and spontaneous polarization in WZ InAs. In QWs, the polarization field in a certain layer can be obtained from the following equation [35]:

$$E_i = \sum_{j=1}^{N} (P_j - P_i) d_j / \varepsilon_j \Big/ \Big(\varepsilon_i \sum_{j=1}^{N} d_j / \varepsilon_j \Big), \quad (2)$$

where i, j is the index of the WZ or ZB layer, N is the total number of layers, ε_i and ε_j are dielectric constants, and d_j is the layer thickness. As a result, the piezopotential V_{piezo} generated by stress regulates the inclination of the band edge and helps to control the TI phase transition. The external stress-induced piezopotential can be obtained as follows:

$$V_{piezo} = E_{piezo} d, \quad (3)$$

where d is the layer thickness in the QW. E_{piezo} can be obtained by the formula (2) without considering P_0 in $P = P_{piezo} + P_0$. The effect of the stress on the polarization field and piezopotential is presented in Fig. 1(d).

The band structures of these WZ/ZB QWs can be obtained from the eight-band $k \cdot p$ Hamiltonians [35,36]. For quantum piezotronic devices based on InAs topological insulators, the edge-state transport property is of vital importance. A direct way to describe the topological insulator and its edge states is a 2D effective Hamiltonian
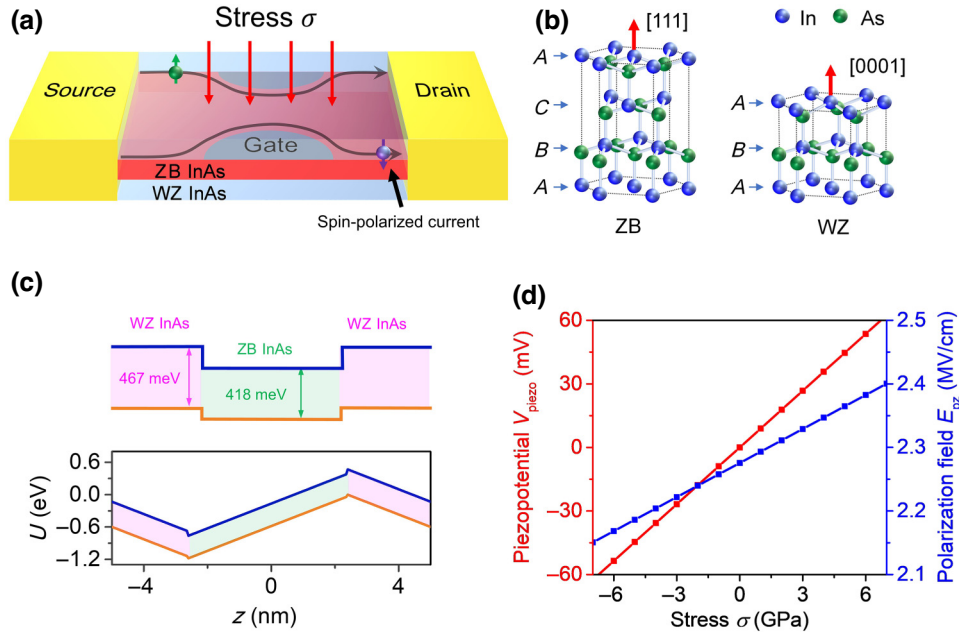

FIG. 1. (a) Quantum point contact in the WZ/ZB InAs topological insulator. The gate potential applied to the split gates controls the width of the QPC and determines the *on* and *off* of edge states. The stress on the QWs regulates the band structure of the TI. (b) Atomic structures of [111] ZB and [0001] WZ. (c) Potential profile of the periodic WZ/ZB InAs QW without (upper) and with (lower) a polarization field. The periodic boundary conditions are taken with a 5-nm thickness of each layer. The total polarization is fixed at 0.0584 C/m^2. (d) Total polarization field versus external stress at a reasonable $P_0 = 0.0584$ C/m^2 and the piezopotential induced by stress in a QW layer of 5-nm width.

TABLE I. Parameters of the effective Hamiltonian at a QW thickness of 5.0 nm.

Parameter	Value
M (meV)	−35.6
B (meV nm^2)	−682.705
D (meV nm^2)	−8.635
A (meV nm)	139.31
α (meV nm)	83.27

[37,38]. This 2D Hamiltonian can be obtained from the eight-band $k \cdot p$ Hamiltonians by performing the Löwdin perturbation technique [39]. The material parameters of WZ and ZB InAs, including the $k \cdot p$ parameters of the eight-band Hamiltonians [40–42], the elastic constants [43], the piezoelectric constants [44], and the spontaneous polarization [26,28,45,46], are presented in the Supplemental Material [47]. Thus, it is possible to calculate the 2D effective Hamiltonian at a given stress and thickness. A four-band 2D effective Hamiltonian is presented at the basis set of $\{|C1, \uparrow\rangle, |H1, \uparrow\rangle, |C1, \downarrow\rangle, |H1, \downarrow\rangle\}$ as follows:

$$
H(k_x, k_y) = \begin{pmatrix} C_k + M_k & Ak_+ & -i\alpha k_- & 0 \\ Ak_- & C_k - M_k & 0 & 0 \\ i\alpha k_+ & 0 & C_k + M_k & -Ak_- \\ 0 & 0 & -Ak_+ & C_k - M_k \end{pmatrix},
$$

(4)

where k_x and k_y are in-plane momentum, $C_k = -Dk^2$, $M_k = M - Bk^2$, $k_\pm = k_x \pm ik_y$, $k^2 = k_+k_-$, and A, B, M, D, α are band parameters. The form of the effective Hamiltonian (4) is the same as the classical Bernevig-Hughes-Zhang (BHZ) model in the HgTe/CdTe QW [48] except for the off-diagonal term $i\alpha k_\pm$, which describes Rashba spin-orbit coupling (RSOC). This RSOC originates from the structural inversion asymmetry induced by the polarization field [49]. Table I lists the band parameters for the WZ/ZB InAs QW at a thickness of $d = 5.0$ nm.

The conductance of WZ/ZB InAs can be given by the Landauer-Büttiker formula [50],

$$
G = \frac{e^2}{h} \sum_{m,n} |T_{mn}|^2,
$$

(5)

where h is the Planck constant. T_{mn} is the coefficient of transmission for the electrons from the mth input transport channel to the nth output transport channel. For quantum piezotronic devices based on TIs, the *on* and *off* states are defined as the conducting and blocking of edge states. Therefore, the edge current of the device at a given source-drain voltage V_{DS} can be calculated as follows [51]:

$$
I = G_0 T_{edge} V_{DS},
$$

(6)

where $G_0 = 2e^2/h$ is the quantum conductance of topological edge states. T_{edge} is the transmission coefficient of the edge state and is controlled by the QPC width of the device. By defining $G = G_0 T_{edge}$, the current I is proportional to the conductance G when V_{DS} is fixed.

Subthreshold swing measures the performance of the FET, including its switching energy efficiency and power loss in the switching and standby states, and the subthreshold swing of the FET can be given as follows [52]:

$$
S = \frac{\partial U_G}{\partial \log_{10}(I)},
$$

(7)

where U_G is the gate voltage and I is the current between the source and drain. When the gate voltage is generated by the split gate potential V_{gate} and the current $I \propto G$, the subthreshold swing in the quantum piezotronic TI device can be expressed as $S = \partial V_{gate}/\partial \log_{10}(G)$ by the split gate potential V_{gate} and conductance G.

III. RESULTS AND DISCUSSION

A. Robust large-gap topological insulator

A TI operating at room temperature is highly desired to broaden device applications [21,53]. An important factor in determining room-temperature TI applications is the band gap Δ, which should be greater than 26 meV ($T = 300$ K) and simultaneously robust to temperature fluctuation. Although a TI with a band gap over 26 meV has been reported in strained HgTe QWs [54], its strong temperature-dependent band structure causes its TI property to be unstable at room temperature [55]. The TI based on the WZ/ZB InAs QW proposed here may be a good candidate to overcome this challenge.

Band inversion indicates a topological phase transition from normal to topological insulator, which is widely confirmed in HgTe/CdTe and InAs/GaSb QWs [37,56]. Figure 2(a) shows the energies of the first electron subband ($C1$) and the first heavy-hole subband ($H1$) as a function of thickness. The inversion of $C1$ and $H1$ occurs at a critical thickness d_c of 4.6 nm. To more clearly show band inversion, we display the band structures of $C1$ and $H1$ at thicknesses d of 4.3 and 5.0 nm in Fig. 2(b). Although both exhibit a band gap, the former is a normal insulator, but the latter is a TI.

Using an effective 2D Hamiltonian or calculating the bulk band of a finite-width strip can lead to inaccuracies in the evaluation of the bulk energy gap, especially in the case of a thin strip where reducing the strip width may increase the bulk band gap [38,57–59]. Using the eight-band $k \cdot p$ Hamiltonian for a planar InAs quantum well, the bulk energy gap is 39 meV, as shown in Fig. 3(a). The band gap $\Delta = 39$ meV is greater than 26 meV ($T = 300$ K), which is important for room-temperature TI applications [21].
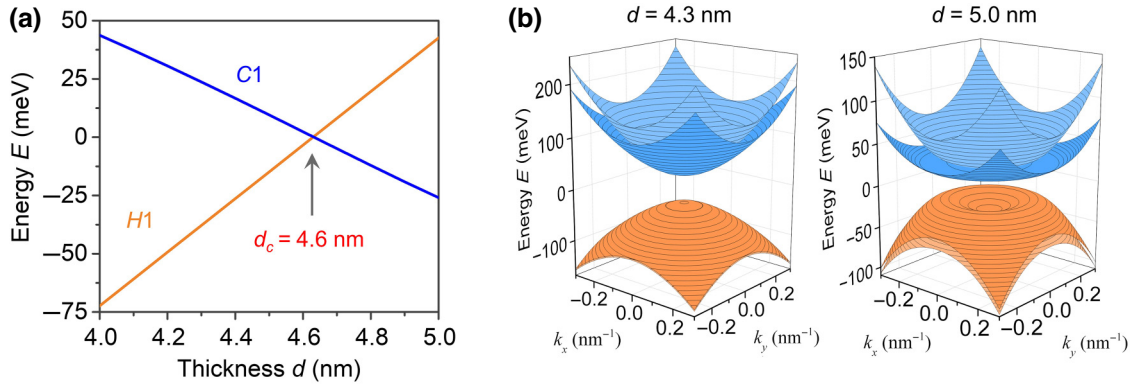
FIG. 2. (a) Reference energy levels of $C1$ and $H1$ versus the QW thickness. The thickness of WZ and ZB is d. (b) Band dispersion of the four-band effective Hamiltonians for the QW widths $d = 4.3$ nm and $d = 5.0$ nm. The spontaneous polarization is 0.051 C/m^2.

Although the proposal of using a polarization field to drive TI states has been demonstrated in several systems, including GaN/InN, GaAs/Ge, and ZnO/CdO QWs [14,32,60], their band gaps are only approximately 10 meV.

Figure 3(b) shows the effect of the built-in electric field on the bulk band gap of TIs. The spontaneous polarization covers the range that has been achieved in the experiments [26,28,45,46]. There are three matter states in the system: normal insulator, TI, and semimetal. Similar to HgTe/CdTe and InAs/GaSb QWs, the increase in thickness induces not only the TI but also the semimetal [56,61]. In the TI state, the band gap increases with the polarization field and reaches 50 meV at a polarization field of 2.72 MV/cm. From the variation trend, this gap may be further increased if the polarization field is continuously increased, which will be discussed in detail in our future work.

A critical magnetic field, in which the edge state can survive, can be used to evaluate the robustness of this TI against magnetic fluctuation [62]. For a WZ/ZB InAs QW TI with thickness d of 5.0 nm and polarization field E of 2.33 MV/cm, this critical magnetic field reaches up to $B_c \approx 33$ T, as observed in the Landau level of Fig. 3(c). This result indicates that the edge states can be preserved with a very large magnetic field and thus are highly robust. Figure 3(d) shows the critical magnetic field as a function of thickness under a fixed polarization field of 2.33 MV/cm. This magnetic field increases with increasing thickness. When the band gap is $\Delta > 26$ meV ($T = 300$ K) at a thickness $d > 4.9$ nm, the critical magnetic field is $B_c > 33$ T. Therefore, room-temperature TI applications based on WZ/ZB InAs QWs are highly robust to magnetic fluctuations. Moreover, the critical magnetic field in this WZ/ZB InAs QW is almost twice as high as that of the three-layer InAs/GaSb QW [63].

The band gap of WZ (ZB) InAs decreases by approximately 43 meV (59 meV) between 0 and 300 K [shown in Fig. 4(a)] [64–66]. The effect of temperature on the band gap of bulk WZ or ZB InAs is significantly higher than that

of InAs TI. To show the effect of temperature, we calculate the bulk band gap of the InAs TI with respect to the temperature in Fig. 4(b). Compared to bulk InAs materials, the energy gap of the InAs TI changes by no more than 9 meV within the temperature range of 0 to 300 K, indicating a weaker temperature sensitivity. Throughout the entire temperature range, the bulk band gap of this 5-nm-wide InAs quantum well TI remains greater than 30 meV. Moreover, as the stress increases to -7 GPa, an increase in the temperature can achieve a large bulk band gap. The weaker temperature sensitivity on the bulk band gap has also been discussed in the multilayer AlSb/GaSb/InAs TI through a comparison with the HgTe/CdHgTe TI having a higher temperature sensitivity [63].

B. Quantum piezotronic transistor with ultralow subthreshold swing

For the quantum piezotronic transistor in Fig. 1(a), we selected the thicknesses of the WZ and ZB layers in the QWs to be 5 nm and the polarization field (without external stress) to be 2.33 MV/cm. Under these circumstances, the band gap remained larger than 26 meV, even with a stress over 9 GPa. The high robustness under a magnetic field was also preserved.

In the QPC region, the potential on the gates controls the width of the QPC. The width of the QPC varies approximately linearly with the gate voltage, as shown in previous experiments [67]. The relationship between the width of the QPC W_{QPC} and the gate potential V_{gate} is given by the following:

$$W_{QPC} = \alpha_{QPC}(V_0 + V_{gate}) + W_0, \quad (8)$$

where V_0 represents the preset bias voltage, and the value of the α parameter is related to the structure of the point-contact region and the material property of the topological insulator. W_0 represents the width of the QPC without potential on the split gates. The parameters used
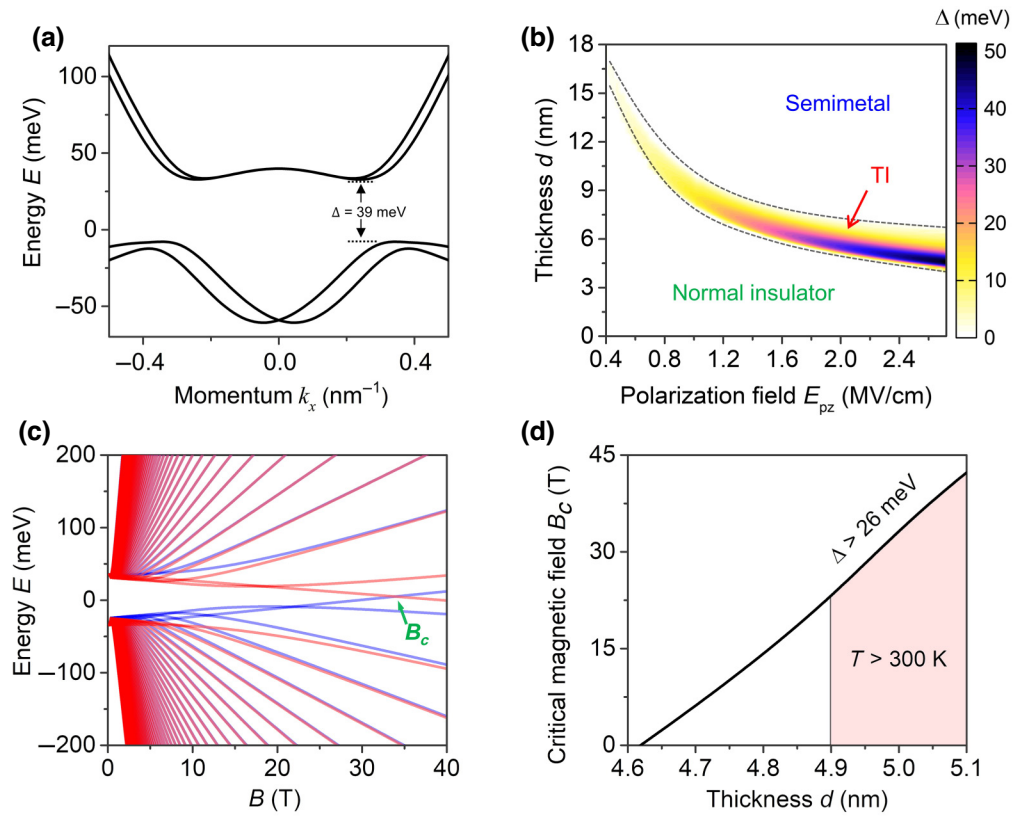
FIG. 3. (a) Band dispersion in the planar InAs quantum well calculated by the eight-band $k \cdot p$ method. (b) Band gap Δ as a function of the total polarization field E_{pz} and QW layer thickness d. (c) Landau levels as a function of magnetic field. (d) Critical magnetic field versus QW width; the red region refers to band gap $\Delta > 26$ meV.

in our calculation are $\alpha_{QPC} = 225$ nm/V, $W_0 = 250$ nm, $V_0 = -0.89$ V [67].

To describe the transport property of the spin-polarized edge state in the switching process, we illustrate the spin current properties injected from the upper-left edge by the KWANT PYTHON package [68]. As shown in Fig. 5(a), when the QPC is wide enough ($W_{QPC} = 40$ nm), the spin current can flow through the QPC region (upper figure). This state

represents the *on* state of the InAs transistor. When the conducting channel is blocked at W_{QPC} of 20 nm (lower figure), the device changes to the *off* state. The Fermi energy is set at $E_F = 5$ meV. The QPC widths W_{QPC} of 40 and 20 nm correspond to V_{gate} values of -43.3 and -132.2 mV, respectively.

In Fig. 5(b), we calculate the conductance of the device (without stress) as a function of gate voltage. The average
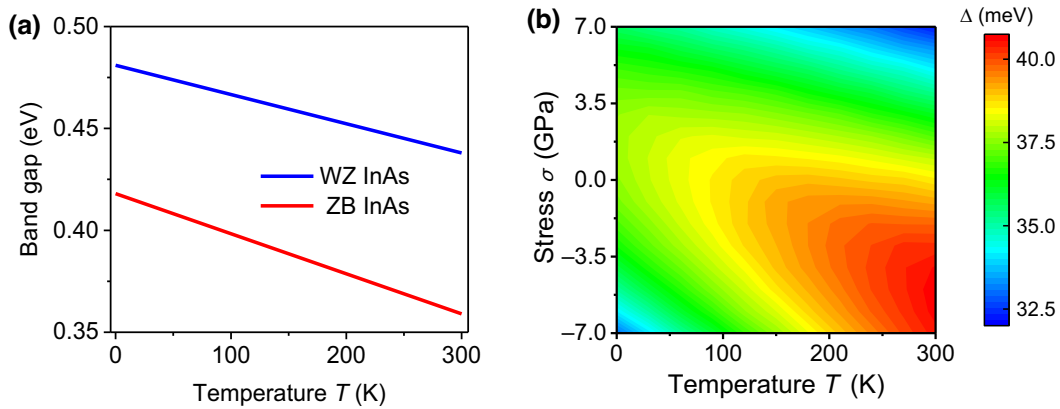

FIG. 4. (a) Band gap of bulk WZ and ZB InAs versus temperature T [64,66]. (b) Bulk band gap Δ of the topological insulator versus stress σ and temperature T. The spontaneous polarization is 0.053 C/m^2, and the layer thickness is 5.0 nm.
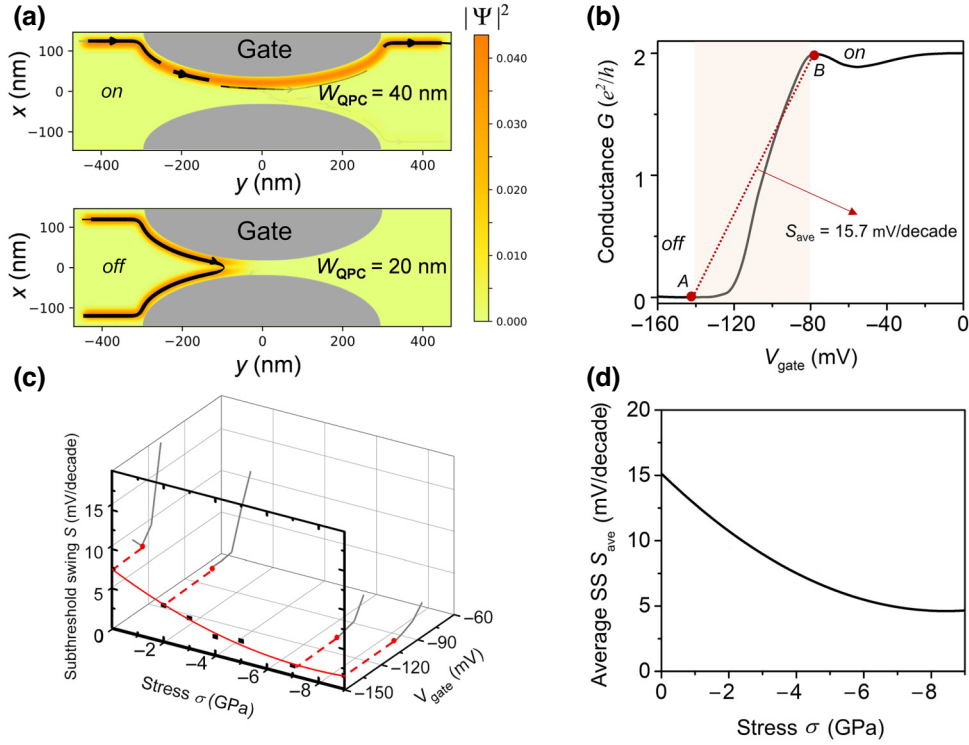
FIG. 5. (a) Spin-polarized current injected from the upper-left edges. The upper figure shows the *on* state of the transport channel and the edge state density at $W_{QPC} = 40$ nm. The lower one shows the *off* state at $W_{QPC} = 20$ nm, and the transport channel is totally blocked by the narrow QPC. (b) Conductance versus gate voltage during the switching process. The light brown region represents the switching from *on* to *off*, with an average subthreshold swing of 15.7 mV/decade. (c) Transient subthreshold swing S varying with the gate potential V_{gate} and stress σ. Stress applied to the QWs helps to reduce the subthreshold swing. (d) Average subthreshold swing S_{ave} in the whole switching process changes with respect to the stress σ. Increasing stress σ can also reduce the average subthreshold swing.

subthreshold swing of the *on-off* process (from *B* to *A*) is $S = 15.7$ mV/decade, and the conductance changes by 4 orders of magnitude. To show that the external stress can regulate the subthreshold swing, the transient subthreshold swing S variations with respect to the gate potential V_{gate} and stress σ are plotted in Fig. 5(c). With increasing stress σ, the minimum value of transient subthreshold swing S gradually decreases.

Further evaluation of the device during the switching process shows that the average subthreshold swing S_{ave} can also be reduced by applying stress. An advantageous value of 5 mV/decade can be obtained when the stress reaches 7 GPa [shown in Fig. 5(d)]. Although increasing the stress to 9 GPa can further reduce the average subthreshold swing, the improvement in the subthreshold swing caused by a larger stress is not evident, and stresses above 7 GPa may also lead to the phase transition of InAs [69]. As in the experiment of piezophototronic *p*-type GaN films [70], stress can be straightforwardly and accurately applied to the samples. This approach has also been used in ultrafast spin lasers [71].

Table II lists some systems that can break the subthreshold swing limitation for comparison. In contrast to these

systems, our InAs topological insulator with QPC proposed has a lower subthreshold swing. Moreover, in the *on* state, the edge channel is robust against local impurities, and the band gap is large enough for room-temperature applications. In addition, interface fluctuations may have little effect on the subthreshold swing of WZ/ZB InAs QWs because the transport properties of the TI with a QPC structure are expected to have a weak dependence on local impurity potentials or rough walls, as discussed in Ref. [38]. A high-quality interface of WZ and ZB InAs is achievable [29]. With these properties, the QPC based on the InAs topological insulator facilitates the design of low power consumption and high-performance piezotronic devices.

IV. SUMMARY

In this study, we investigated the impact of polarization on the topological properties of WZ/ZB InAs QWs. Polarization triggered the TI with a larger bulk band gap of approximately 50 meV, which was accessible to room-temperature applications. For an FET based on WZ/ZB InAs QWs, the subthreshold swing could be reduced to

TABLE II.   Comparison of subthreshold swing S.

Material	Mechanism	S^a (mV/decade)
MoS_2/Ge	Tunneling field effect	31.1 [72]
Black phosphorus		22.9 [73]
$CuInP_2S_6/MoS_2$	Negative capacity	28 [74] (minimum)
$WSe_2/Hf_{0.5}Zr_{0.5}O_2$		27.8 [75]
MoS_2/graphene	Dirac source	33.5 [76]
Piezo WZ/ZB InAs	QPC based on TI	5.0 (this work)

^{a}Average subthreshold swing, excluding the data marked as the minimum value.

5 mV/decade under a 7-GPa stress. This work provides an alternative strategy to design low power consumption and high-performance room-temperature quantum piezotronic transistors based on polycrystalline QWs.

[1] Z. L. Wang, Progress in piezotronics and piezo-phototronics, Adv. Mater. **24**, 4632 (2012).

[2] W. Wu and Z. L. Wang, Piezotronics and piezo-phototronics for adaptive electronics and optoelectronics, Nat. Rev. Mater. **1**, 1 (2016).

[3] Z. L. Wang, Self-powered nanosensors and nanosystems, Adv. Mater. **24**, 280 (2012).

[4] Y. Zhang, Y. Liu, and Z. L. Wang, Fundamental theory of piezotronics, Adv. Mater. **23**, 3004 (2011).

[5] Q. Lai, L. Zhu, Y. Pang, L. Xu, J. Chen, Z. Ren, J. Luo, L. Wang, L. Chen, K. Han, et al., Piezo-phototronic effect enhanced photodetector based on $CH_3NH_3PbI_3$ single crystals, ACS Nano **12**, 10501 (2018).

[6] J. Sun, Q. Hua, R. Zhou, D. Li, W. Guo, X. Li, G. Hu, C. Shan, Q. Meng, L. Dong, et al., Piezo-phototronic effect enhanced efficient flexible perovskite solar cells, ACS Nano **13**, 4507 (2019).

[7] Z. L. Wang and J. Song, Piezoelectric nanogenerators based on zinc oxide nanowire arrays, Science **312**, 242 (2006).

[8] J. Zhou, Y. Gu, P. Fei, W. Mai, Y. Gao, R. Yang, G. Bao, and Z. L. Wang, Flexible piezotronic strain sensor, Nano Lett. **8**, 3035 (2008).

[9] X. Wang, J. Zhou, J. Song, J. Liu, N. Xu, and Z. L. Wang, Piezoelectric field effect transistor and nanoforce sensor based on a single ZnO nanowire, Nano Lett. **6**, 2768 (2006).

[10] Q. Yang, W. Wang, S. Xu, and Z. L. Wang, Enhancing light emission of ZnO microwire-based diodes by piezo-phototronic effect, Nano Lett. **11**, 4012 (2011).

[11] W. Wu, X. Wen, and Z. L. Wang, Taxel-addressable matrix of vertical-nanowire piezotronic transistors for active and adaptive tactile imaging, Science **340**, 952 (2013).

[12] C. An, H. Qi, L. Wang, X. Fu, A. Wang, Z. L. Wang, and J. Liu, Piezotronic and piezo-phototronic effects of atomically-thin ZnO nanosheets, Nano Energy **82**, 105653 (2021).

[13] G. Hu, Y. Zhang, L. Li, and Z. L. Wang, Piezotronic transistor based on topological insulators, ACS Nano **12**, 779 (2018).

[14] G. Hu and Y. Zhang, Quantum piezotronic devices based on ZnO/CdO quantum well topological insulator, Nano Energy **77**, 105154 (2020).

[15] M. Fu, M. Dan, G. Hu, L. Li, and Y. Zhang, Polarization-induced ultrahigh Rashba spin-orbit interaction in ZnO/CdO quantum well, Nano Energy **88**, 106310 (2021).

[16] G. Nazir, A. Rehman, and S. J. Park, Energy-efficient tunneling field-effect transistors for low-power device applications: Challenges and opportunities, ACS Appl. Mater. Interfaces. **12**, 47127 (2020).

[17] A. M. Ionescu and H. Riel, Tunnel field-effect transistors as energy-efficient electronic switches, Nature **479**, 329 (2011).

[18] M. Hoffmann, S. Slesazeck, U. Schroeder, and T. Mikolajick, What's next for negative capacitance electronics?, Nat. Electron. **3**, 504 (2020).

[19] Z. Qin, Z. Wei, and A. Seabaugh, Low-subthreshold-swing tunnel transistors, IEEE Electron Device Lett. **27**, 297 (2006).

[20] M. Nadeem, I. Di Bernardo, X. Wang, M. S. Fuhrer, and D. Culcer, Overcoming Boltzmann's tyranny in a transistor via the topological quantum field effect, Nano Lett. **21**, 3155 (2021).

[21] A. Molle, J. Goldberger, M. Houssa, Y. Xu, S. C. Zhang, and D. Akinwande, Buckled two-dimensional Xene sheets, Nat. Mater. **16**, 163 (2017).

[22] A. K. Tareen, K. Khan, M. Aslam, H. Zhang, and X. Liu, Recent progress, challenges, and prospects in emerging group-VIA Xenes: Synthesis, properties and novel applications, Nanoscale **13**, 510 (2021).

[23] H. Riel, L.-E. Wernersson, M. Hong, and J. A. del Alamo, III–V compound semiconductor transistors—from planar to nanowire structures, MRS Bull. **39**, 668 (2014).

[24] J. Seidl, J. G. Gluschke, X. Yuan, H. H. Tan, C. Jagadish, P. Caroff, and A. P. Micolich, Postgrowth shaping and transport anisotropy in two-dimensional InAs nanofins, ACS Nano **15**, 7226 (2021).

[25] P. Staudinger, K. E. Moselund, and H. Schmid, Exploring the size limitations of wurtzite III–V film growth, Nano Lett. **20**, 686 (2020).

[26] L. Li, Z. Gan, M. R. McCartney, H. Liang, H. Yu, W. J. Yin, Y. Yan, Y. Gao, J. Wang, and D. J. Smith, Determination of polarization-fields across polytype interfaces in InAs nanopillars, Adv. Mater. **26**, 1052 (2014).

[27] M. Moller, M. M. de Lima, Jr., A. Cantarero, T. Chiara-monte, M. A. Cotta, and F. Iikawa, Optical emission of InAs nanowires, Nanotechnology **23,** 375704 (2012).

[28] J. Becker, S. Morkötter, J. Treu, M. Sonner, M. Speck-bacher, M. Döblinger, G. Abstreiter, J. J. Finley, and G. Koblmüller, Carrier trapping and activation at short-period wurtzite/zinc-blende stacking sequences in polytypic InAs nanowires, Phys. Rev. B **97,** 115306 (2018).

[29] K. A. Dick, C. Thelander, L. Samuelson, and P. Caroff, Crystal phase engineering in single InAs nanowires, Nano Lett. **10,** 3494 (2010).

[30] L. B. Zhang, F. Cheng, F. Zhai, and K. Chang, Electrical switching of the edge channel transport in HgTe quantum wells with an inverted band structure, Phys. Rev. B **83,** 081402 (2011).

[31] J. Bao, D. C. Bell, F. Capasso, N. Erdman, D. Wei, L. Fröberg, T. Mårtensson, and L. Samuelson, Nanowire-induced wurtzite InAs thin film on zinc-blende InAs sub-strate, Adv. Mater. **21,** 3654 (2009).

[32] M. S. Miao, Q. Yan, C. G. Van de Walle, W. K. Lou, L. L. Li, and K. Chang, Polarization-Driven Topological Insu-lator Transition in a GaN/InN/GaN Quantum Well, Phys. Rev. Lett. **109,** 186803 (2012).

[33] C. Mailhiot and D. L. Smith, Electronic structure of [001]- and [111]-growth-axis semiconductor superlattices, Phys. Rev. B: Condens. Matter **35,** 1242 (1987).

[34] D. L. Smith and C. Mailhiot, Theory of semiconductor superlattice electronic structure, Rev. Mod. Phys. **62,** 173 (1990).

[35] P. E. Faria Junior and G. M. Sipahi, Band structure calcu-lations of InP wurtzite/zinc-blende quantum wells, J. Appl. Phys. **112,** 103716 (2012).

[36] P. E. Faria Junior, T. Campos, and G. M. Sipahi, Interband polarized absorption in InP polytypic superlattices, J. Appl. Phys. **116,** 193501 (2014).

[37] M. Z. Hasan and C. L. Kane, Colloquium: Topological insulators, Rev. Mod. Phys. **82,** 3045 (2010).

[38] V. Krueckl and K. Richter, Switching Spin and Charge between Edge States in Topological Insulator Constrictions, Phys. Rev. Lett. **107,** 086803 (2011).

[39] P. O. Löwdin, A note on the quantum-mechanical perturba-tion theory, J. Chem. Phys. **19,** 1396 (1951).

[40] P. E. Faria Junior, T. Campos, C. M. O. Bastos, M. Gmi-tra, J. Fabian, and G. M. Sipahi, Realistic multiband $k \cdot p$ approach from *ab initio* and spin-orbit coupling effects of InAs and InP in wurtzite phase, Phys. Rev. B **93,** 235204 (2016).

[41] C. Pryor, Eight-band calculations of strained InAs/GaAs quantum dots compared with one-, four-, and six-band approximations, Phys. Rev. B **57,** 7190 (1998).

[42] S. B. Radhia, N. Fraj, I. Saidi, and K. Boujdaria, The eight-level k · p model for the conduction and valence bands of InAs, InP, InSb, Semicond. Sci. Technol. **22,** 427 (2007).

[43] M. W. Larsson, J. B. Wagner, M. Wallin, P. Håkans-son, L. E. Fröberg, L. Samuelson, and L. R. Wallenberg, Strain mapping in free-standing heterostructured wurtzite InAs/InP nanowires, Nanotechnology **18,** 015504 (2007).

[44] F. Boxberg, N. Sondergaard, and H. Q. Xu, Elastic and piezoelectric properties of zincblende and wurtzite

crystalline nanowire heterostructures, Adv. Mater. **24,** 4692 (2012).

[45] I. J. Chen, S. Lehmann, M. Nilsson, P. Kivisaari, H. Linke, K. A. Dick, and C. Thelander, Conduction band offset and polarization effects in InAs nanowire polytype junctions, Nano Lett. **17,** 902 (2017).

[46] S. A. Dayeh, D. Susac, K. L. Kavanagh, E. T. Yu, and D. Wang, Structural and room-temperature transport prop-erties of zinc blende and wurtzite InAs nanowires, Adv. Funct. Mater. **19,** 2102 (2009).

[47] See Supplemental Material at http://link.aps.org/supple mental/10.1103/PhysRevApplied.20.014061 for eight-band Hamiltonian and parameters.

[48] M. Konig, S. Wiedmann, C. Brune, A. Roth, H. Buhmann, L. W. Molenkamp, X. L. Qi, and S. C. Zhang, Quantum spin Hall insulator state in HgTe quantum wells, Science **318,** 766 (2007).

[49] B. Büttner, C. X. Liu, G. Tkachov, E. G. Novik, C. Brüne, H. Buhmann, E. M. Hankiewicz, P. Recher, B. Trauzettel, S. C. Zhang, *et al.*, Single valley Dirac fermions in zero-gap HgTe quantum wells, Nat. Phys. **7,** 418 (2011).

[50] R. Landauer, Electrical transport in open and closed sys-tems, Z. Med. Phys. **68,** 217 (1987).

[51] S. Datta, *Quantum Transport: Atom to Transistor* (Cam-bridge university press, Cambridge, 2005).

[52] Y. Zhai, Z. Feng, Y. Zhou, and S. T. Han, Energy-efficient transistors: Suppressing the subthreshold swing below the physical limit, Mater. Horizons **8,** 1601 (2021).

[53] A. Wang, Z. Wang, A. Du, and M. Zhao, Band inversion and topological aspects in a TiNI monolayer, Phys. Chem. Chem. Phys. **18,** 22154 (2016).

[54] P. Leubner, L. Lunczer, C. Brune, H. Buhmann, and L. W. Molenkamp, Strain Engineering of the Band Gap of HgTe Quantum Wells Using Superlattice Virtual Sub-strates, Phys. Rev. Lett. **117,** 086403 (2016).

[55] M. Marcinkiewicz, S. Ruffenach, S. S. Krishtopenko, A. M. Kadykov, C. Consejo, D. B. But, W. Desrat, W. Knap, J. Torres, A. V. Ikonnikov, *et al.*, Temperature-driven single-valley Dirac fermions in HgTe quantum wells, Phys. Rev. B **96,** 035405 (2017).

[56] C. Liu, T. L. Hughes, X. L. Qi, K. Wang, and S. C. Zhang, Quantum Spin Hall Effect in Inverted Type-II Semiconduc-tors, Phys. Rev. Lett. **100,** 236601 (2008).

[57] J. Li, S. Sanz, N. Merino-Diez, M. Vilas-Varela, A. Garcia-Lekue, M. Corso, D. G. de Oteyza, T. Frederiksen, D. Pena, and J. I. Pascual, Topological phase transition in chiral graphene nanoribbons: From edge bands to end states, Nat. Commun. **12,** 5538 (2021).

[58] See Supplemental Material at http://link.aps.org/supple mental/10.1103/PhysRevApplied.20.014061 for the evalu-ation of the good accuracy of the effective 2D effective Hamiltonian.

[59] P. C. Klipstein, Structure of the quantum spin Hall states in HgTe/CdTe and InAs/GaSb/AlSb quantum wells, Phys. Rev. B **91,** 035310 (2015).

[60] D. Zhang, W. Lou, M. Miao, S. C. Zhang, and K. Chang, Interface-Induced Topological Insulator Transition in GaAs/Ge/GaAs Quantum Wells, Phys. Rev. Lett. **111,** 156402 (2013).

[61] B. A. Bernevig, T. L. Hughes, and S. C. Zhang, Quantum spin Hall effect and topological phase transition in HgTe quantum wells, Science **314,** 1757 (2006).

[62] S.-B. Zhang, Y.-Y. Zhang, and S.-Q. Shen, Robustness of quantum spin Hall effect in an external magnetic field, Phys. Rev. B **90,** 115305 (2014).

[63] S. S. Krishtopenko and F. Teppe, Quantum spin Hall insulator with a large bandgap, Dirac fermions, and bilayer graphene analog, Sci. Adv. **4,** eaap7529 (2018).

[64] S. Pournia, S. Linser, G. Jnawali, H. E. Jackson, L. M. Smith, A. Ameruddin, P. Caroff, J. Wong-Leung, H. H. Tan, C. Jagadish, *et al.*, Exploring the band structure of Wurtzite InAs nanowires using photocurrent spectroscopy, Nano Res. **13,** 1586 (2020).

[65] I. Vurgaftman, J. R. Meyer, and L. R. Ram-Mohan, Band parameters for III–V compound semiconductors and their alloys, J. Appl. Phys. **89,** 5815 (2001).

[66] N. Bouarissa and H. Aourag, The temperature dependence of the band gaps in narrow-gap semiconductors, Infrared Phys. Technol. **38,** 153 (1997).

[67] B. J. van Wees, H. van Houten, C. W. Beenakker, J. G. Williamson, L. P. Kouwenhoven, D. van der Marel, and C. T. Foxon, Quantized Conductance of Point Contacts in a Two-Dimensional Electron Gas, Phys. Rev. Lett. **60,** 848 (1988).

[68] C. W. Groth, M. Wimmer, A. R. Akhmerov, and X. Waintal, Kwant: A software package for quantum transport, New J. Phys. **16,** 063065 (2014).

[69] Y. K. Vohra, S. T. Weir, and A. L. Ruoff, High-pressure phase transitions and equation of state of the III–V compound InAs up to 27 GPa, Phys. Rev. B: Condens. Matter **31,** 7344 (1985).

[70] Y. Hu, Y. Zhang, L. Lin, Y. Ding, G. Zhu, and Z. L. Wang, Piezo-phototronic effect on electroluminescence properties of p-type GaN thin films, Nano Lett. **12,** 3851 (2012).

[71] M. Lindemann, G. Xu, T. Pusch, R. Michalzik, M. R. Hofmann, I. Zutic, and N. C. Gerhardt, Ultrafast spin-lasers, Nature **568,** 212 (2019).

[72] D. Sarkar, X. Xie, W. Liu, W. Cao, J. Kang, Y. Gong, S. Kraemer, P. M. Ajayan, and K. Banerjee, A subthermionic tunnel field-effect transistor with an atomically thin channel, Nature **526,** 91 (2015).

[73] S. Kim, G. Myeong, W. Shin, H. Lim, B. Kim, T. Jin, S. Chang, K. Watanabe, T. Taniguchi, and S. Cho, Thickness-controlled black phosphorus tunnel field-effect transistor for low-power switches, Nat. Nanotechnol. **15,** 203 (2020).

[74] X. Wang, P. Yu, Z. Lei, C. Zhu, X. Cao, F. Liu, L. You, Q. Zeng, Y. Deng, C. Zhu, *et al.*, Van der Waals negative capacitance transistors, Nat. Commun. **10,** 3037 (2019).

[75] M. Si, C. Jiang, W. Chung, Y. Du, M. A. Alam, and P. D. Ye, Steep-slope WSe2 negative capacitance field-effect transistor, Nano Lett. **18,** 3682 (2018).

[76] Z. Tang, C. Liu, X. Huang, S. Zeng, L. Liu, J. Li, Y. G. Jiang, D. W. Zhang, and P. Zhou, A steep-slope MoS2/graphene Dirac-source field-effect transistor with a large drive current, Nano Lett. **21,** 1758 (2021).